



# The origin of hematite nanowire growth during the thermal oxidation of iron

Lu Yuan<sup>a</sup>, Yiqian Wang<sup>b</sup>, Rongsheng Cai<sup>b</sup>, Qike Jiang<sup>c</sup>, Jianbo Wang<sup>c</sup>, Boquan Li<sup>d</sup>, Anju Sharma<sup>e</sup>, Guangwen Zhou<sup>a,\*</sup>

<sup>a</sup> Department of Mechanical Engineering & Multidisciplinary Program in Materials Science and Engineering, State University of New York, Binghamton, NY 13902, United States

<sup>b</sup> The Cultivation Base for State Key Laboratory, Qingdao University, Qingdao 266071, China

<sup>c</sup> School of Physics, Center for Electron Microscopy and MOE Key Laboratory of Artificial Micro- and Nano-Structures, Wuhan University, Wuhan 430072, China

<sup>d</sup> Materials Science and Engineering Program, Worcester Polytechnic Institute, Worcester, MA 01609, United States

<sup>e</sup> Small Scale Systems Integration and Packaging Center, State University of New York, Binghamton, NY 13902, United States

## ARTICLE INFO

### Article history:

Received 29 July 2011

Received in revised form

19 November 2011

Accepted 23 December 2011

Available online 9 January 2012

### Keywords:

Iron

Oxidation

Hematite (Fe<sub>2</sub>O<sub>3</sub>)

Magnetite (Fe<sub>3</sub>O<sub>4</sub>)

Wustite (FeO)

Nanowires

Stress

## ABSTRACT

The oxidation of Fe in pure oxygen between 400 °C and 600 °C has been investigated in order to obtain insight into the mechanism of the spontaneous formation of  $\alpha$ -Fe<sub>2</sub>O<sub>3</sub> nanowires. By varying the oxidation temperature, Fe can be oxidized to form Fe<sub>2</sub>O<sub>3</sub>/Fe<sub>3</sub>O<sub>4</sub>/FeO/Fe or Fe<sub>2</sub>O<sub>3</sub>/Fe<sub>3</sub>O<sub>4</sub>/Fe layered structure, followed by hematite nanowire growth on the outer layer of hematite (Fe<sub>2</sub>O<sub>3</sub>). It is observed that Fe<sub>2</sub>O<sub>3</sub> nanowires have a bicrystal structure and form directly on the top of the underlying Fe<sub>2</sub>O<sub>3</sub> grains. It is shown that the compressive stresses generated by the volume change accompanying the Fe<sub>2</sub>O<sub>3</sub>/Fe<sub>3</sub>O<sub>4</sub> interface reaction stimulate Fe<sub>2</sub>O<sub>3</sub> nanowire formation and that the Fe<sub>2</sub>O<sub>3</sub> nanowire growth is via surface diffusion of Fe cations supplied from the outward grain boundary diffusion through the Fe<sub>2</sub>O<sub>3</sub> layer. This principle of nanowire formation may have broader applicability in layered systems, where the stress gradient in thin layers can be introduced via solid-state interfacial reaction or other means.

© 2011 Elsevier B.V. All rights reserved.

## 1. Introduction

Hematite ( $\alpha$ -Fe<sub>2</sub>O<sub>3</sub>) is the most stable iron oxide under ambient conditions. It is a semiconductor with a band gap of 2.1 eV, and has high resistivity to corrosion and low toxicity [1]. A significant effort has been focused on synthesis of nanostructured  $\alpha$ -Fe<sub>2</sub>O<sub>3</sub> due to its great potential for a wide range of applications, including serving as catalysts [2], gas sensors, electrode materials [3], and magnetic recording media [4]. Because of its technical simplicity, the thermal oxidation of iron in an oxygen containing atmosphere has recently received considerable attention as an effective approach for large-scale synthesis of high-quality  $\alpha$ -Fe<sub>2</sub>O<sub>3</sub> nanowires (NWs) [5–16]. The phenomenon of oxide NW formation from the oxidation of metals is not limited to Fe, similar dense populations of oxide NWs (or whisker, blades, belts) have been extensively described in the oxidation of other metals such as Cu [17–21] and Zn [22]. Oxide whisker growth in relation with metal oxidation has long been observed; however, a satisfactory growth mechanism for the formation of these one-dimensional oxide structures has not yet

been established. The required experimental evidence to sustain a specific growth mechanism is still very few.

Several mechanisms have been invoked to account for the one-dimensional oxide NW growth as schematically shown in Fig. 1. (a) Evaporation and condensation [23,24], (b) fast internal diffusion along a tunnel centered on the core of a screw dislocation [25,26], and (c) surface diffusion along the sides of nanowires [27]. It is now widely accepted that the first of these does not apply for obvious reasons of the requirement for the formation of highly volatile species, which usually does not occur for the intermediate oxidation temperatures at which hematite nanowires grow. In light of recent electron microscopy observations revealing that  $\alpha$ -Fe<sub>2</sub>O<sub>3</sub> NWs have a bicrystal or single crystal structure (i.e., no hollow pipe present along the axial core of NWs), the scenario of the fast internal diffusion mechanism is also debated [9,10,28,29]. By examining CuO NW growth during the oxidation of Cu, we have shown recently that the compressive stresses generated from the CuO/Cu<sub>2</sub>O interfacial reaction serves as the driving force to stimulate CuO NW growth, where the surface diffusion of Cu cations on the NW sidewall controls the NW uniaxial growth kinetics [30,31]. In the present work we present a systematic investigation of Fe<sub>2</sub>O<sub>3</sub> NW growth during the oxidation of Fe. Our results indicate that the driving force for hematite NW formation is related to the

\* Corresponding author. Tel.: +1 607777 5084; fax: +1 607777 4620.

E-mail address: [gzhou@binghamton.edu](mailto:gzhou@binghamton.edu) (G. Zhou).

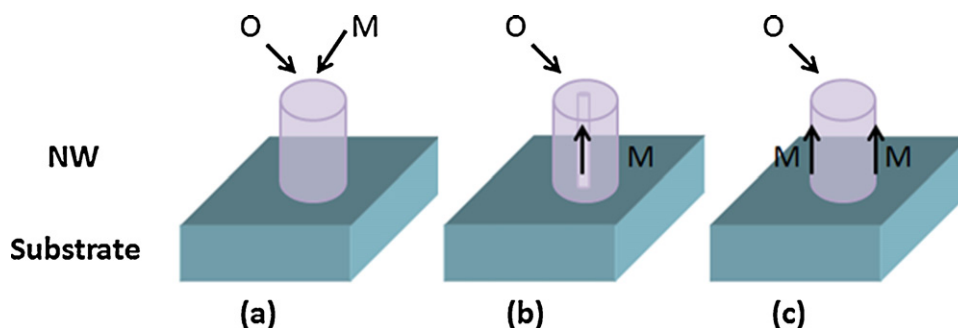


**Fig. 1.** Comparison of the various mechanisms proposed for oxide nanowire growth during the oxidation of metals: (a) evaporation and condensation; (b) internal diffusion along the core of a screw dislocation; (c) surface diffusion along the sidewall of a nanowire.

compressive stresses generated by the  $\text{Fe}_2\text{O}_3/\text{Fe}_3\text{O}_4$  interfacial reaction and the one-dimensional growth kinetics is governed by the surface diffusion of Fe, whereby demonstrating a greater universality of the principle of stress-driven oxide NW formation during the oxidation of metals.

## 2. Materials and methods

High-purity iron foils (99.99% purity) are first thoroughly rinsed with deionized water followed by ultrasonication in acetone for 5 min. The cleaned iron substrates are then placed on a substrate heater in the vacuum chamber and the sample temperature is monitored using a K-type thermocouple in contact with the sample heater. The chamber is pumped to vacuum ( $\sim 2 \times 10^{-6}$  Torr), and then filled with 200 Torr oxygen pressure (the purity of oxygen is 99.999%). The chamber is then sealed and the Fe sample is heated to the desired temperature (400 °C and 600 °C) at 20 °C/min in the oxygen gas. After the Fe sample is oxidized for different durations (from 30 min to 4 h), it is then cooled down in the same oxygen atmosphere to room temperature at the rate of  $\sim 10$  °C/min. Growth morphology and chemical composition of the oxidized samples are examined using a field emission scanning electron microscopy (FEG-SEM, FEI Supra 55VP), atomic force microscopy (AFM), and X-ray photoelectron spectroscopy (XPS). Length and diameter of hematite NWs are measured from cross-sectional SEM images. Cross-sectional transmission electron microscopy (TEM) specimens are made from the oxidized Fe foils. The microstructures and crystallographic orientation of grains of multi-layered  $\text{FeO}/\text{Fe}_3\text{O}_4/\text{Fe}_2\text{O}_3/\text{Fe}_2\text{O}_3$ -NWs are analyzed using a JEOL 2100F TEM operated at 200 kV.

## 3. Results

Oxide NWs are formed on Fe substrates for the oxidation temperatures examined (400 °C and 600 °C). Fig. 2 shows representative SEM images of the general morphology of the Fe substrates oxidized at 400 °C and 600 °C, respectively, for 1 h under the oxygen pressure of 200 Torr. Oxide NWs are observed for both the oxidation temperatures and NWs are relatively perpendicular to the Fe substrate. It is observed that the NW density is significantly enhanced at the higher oxidation temperature. In addition, both the NW diameter and length increase with the oxidation temperature. At 400 °C, the NW diameter is about 50 nm and lengths range from 100 nm to 2  $\mu\text{m}$ . At 600 °C, the NWs diameters vary from 50 nm to 150 nm and the average length range is about 5  $\mu\text{m}$ . Oxide NWs for both the oxidation temperatures have a tapered shape at the tip, as shown in the inset images in Fig. 2.

SEM investigation of the cross-section part of the oxidized Fe samples reveals the formation of different oxide layer structures for the NW growth at the two oxidation temperatures. Fig. 3 shows the cross-sectional SEM images of the Fe foils oxidized at 400 °C and 600 °C, respectively. The oxidation at 400 °C results in the formation of two oxide layers with a  $\sim 2$   $\mu\text{m}$  thick inner layer in contact with the Fe substrate and a  $\sim 250$  nm thick outer layer in contact with the roots of oxide NWs. Using X-ray energy dispersive spectroscopy (EDS) analysis, as shown in Fig. 2(c), these oxide layers can be easily identified as magnetite ( $\text{Fe}_3\text{O}_4$ ) and hematite ( $\text{Fe}_2\text{O}_3$ ) with  $\text{Fe}_3\text{O}_4$  being the bottom layer and  $\text{Fe}_2\text{O}_3$  being the outer layer and the oxide NWs, respectively. The oxide scale formed at 600 °C consists of three layers with a much thicker ( $\sim 5$   $\mu\text{m}$ ) inner FeO layer that lies directly above the Fe substrate, an intermediate  $\text{Fe}_3\text{O}_4$  layer ( $\sim 2$   $\mu\text{m}$ ), and a thin outer  $\text{Fe}_2\text{O}_3$  layer ( $\sim 400$  nm).

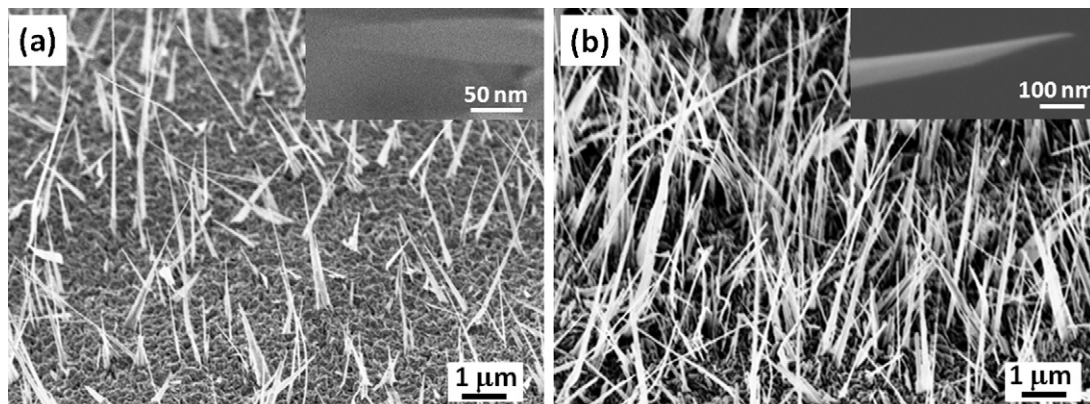


**Fig. 2.** SEM micrographs of the surface morphology of Fe substrates oxidized at (a) 400 °C and (b) 600 °C for 1 h under the oxygen pressure of 200 Torr.

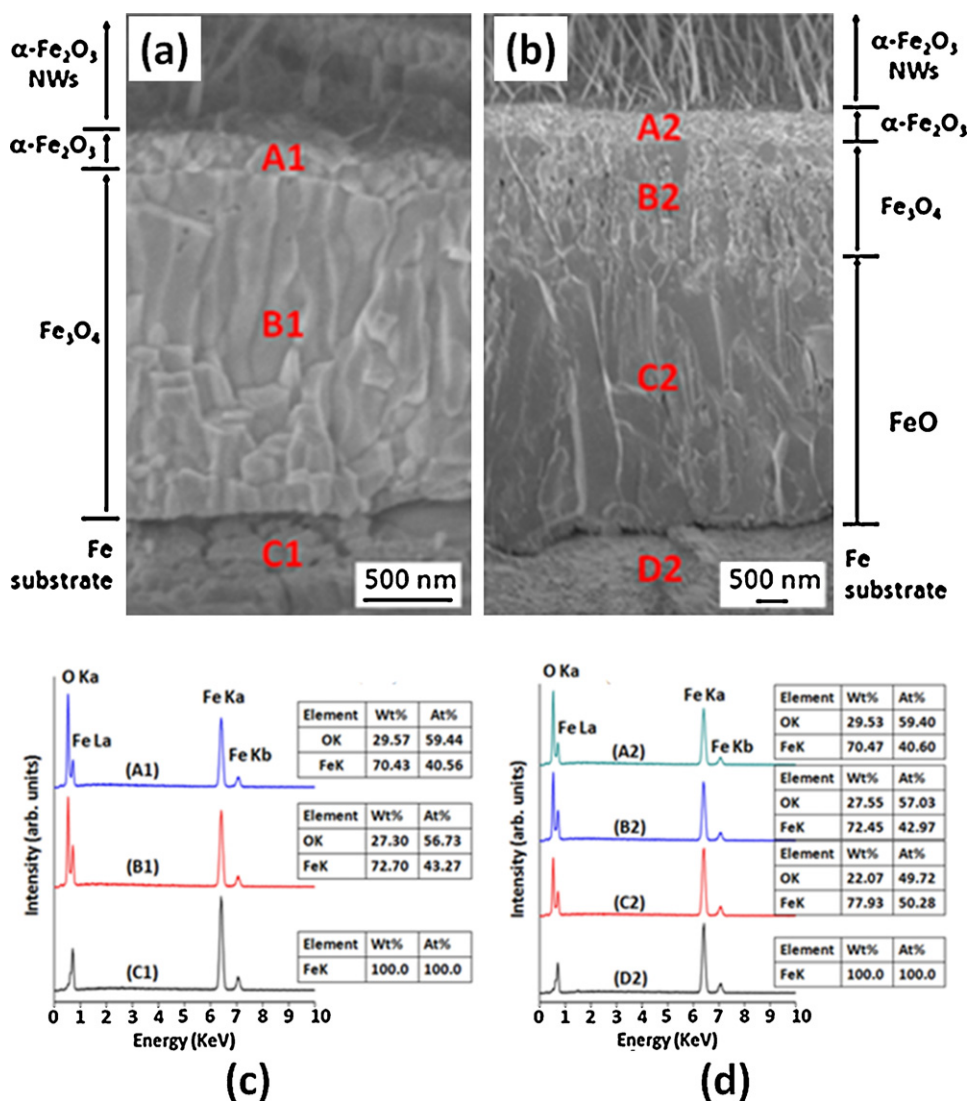


**Fig. 3.** Cross-sectional SEM images of Fe substrates oxidized at (a) 400 °C; (b) 600 °C; the oxidation at 400 °C results in the growth of a two-layered oxide scale structure while the oxidation at 600 °C leads to the growth of a three-layered oxide structure; (c) EDS spectra and the compositions from the regions of A1, B1, C1, as indicated in Fig. 2a; (d) EDS spectra and the compositions from the regions of A2, B2, C2, D2 shown in Fig. 2b.

thick) on which  $\text{Fe}_2\text{O}_3$  NWs are formed, as determined by EDS measurements shown in Fig. 2(d). Several features can be noted from these observations: (1) the thickness of the outer  $\text{Fe}_2\text{O}_3$  layer only changes relatively moderately from 250 nm to 400 nm, irrespective of the dramatic increase (from 2  $\mu\text{m}$  to 7  $\mu\text{m}$ ) in the thickness of the underlying oxide layers for the higher oxidation temperature. In addition, our SEM examination of samples with different oxidation durations reveals that the prolonged oxidation leads to no significant changes in the thickness of the  $\text{Fe}_2\text{O}_3$  layer, suggesting an inherent requirement for the thickness of the  $\text{Fe}_2\text{O}_3$  layer for oxide NW formation during the oxidation; (2) the thin layer of  $\text{Fe}_2\text{O}_3$  is required for  $\text{Fe}_2\text{O}_3$  NW growth but the FeO phase in the bottom layer is not essential; (3) the inner oxide layers ( $\text{Fe}_3\text{O}_4$  for oxidation at 400 °C and  $\text{Fe}_3\text{O}_4$  and FeO at 600 °C) are composed of coarse columnar grains perpendicular to the Fe base whereas the outer  $\text{Fe}_2\text{O}_3$  layer consists of considerably fine grains. A noticeable trend is that the thickness and grain size of oxide layers decrease sequentially across the oxide layers from FeO to  $\text{Fe}_3\text{O}_4$  and then to  $\text{Fe}_2\text{O}_3$ .

To confirm the formation of an  $\alpha\text{-Fe}_2\text{O}_3$  phase, XPS measurement was performed on the Fe samples oxidized at the two temperatures. From Fig. 4a, we can see that the XPS spectra

obtained from nanowires formed from the two oxidation temperatures exhibit the same feature, suggesting the same form of existence of Fe and O in the two samples. The  $\text{Fe}2\text{p}$  spectra of the oxide nanowires (Fig. 4b) show the binding energies of 724.2 (Fe 2p<sub>1/2</sub>) and 710.2 eV (Fe 2p<sub>3/2</sub>) with a shake-up satellite line at 719.2 eV, which are characteristic for  $\text{Fe}^{3+}$  in  $\text{Fe}_2\text{O}_3$ . The peak positions and shape of these peaks also agree well with those of the  $\text{Fe}^{3+}$  oxidation state reported [8,32]. The O1s peak shown in Fig. 4c at the binding energy of 530.1 eV confirms the oxidation state of  $\text{O}^{2-}$  in the oxide, and the second broad peak feature at 531.8 eV can be attributed to  $\text{OH}^-$  or absorbed oxygen [8].

Since growth of  $\text{Fe}_2\text{O}_3$  NWs occurs on the outer  $\text{Fe}_2\text{O}_3$  layer, closer-views from the interface areas between the  $\text{Fe}_2\text{O}_3$  layer and the NW root regions are made, as shown in Fig. 5a. It can be seen that  $\text{Fe}_2\text{O}_3$  NWs are formed on the top of  $\text{Fe}_2\text{O}_3$  grains rather than at grain boundary (GB) areas. To further confirm that  $\text{Fe}_2\text{O}_3$  NWs are formed directly on individual  $\text{Fe}_2\text{O}_3$  grains, the Fe substrate is oxidized for a short time so that their initial growth morphology could be observed. Fig. 5b shows a representative SEM image of a Fe surface oxidized at 400 °C for 30 min. It is visible that the oxidized surface consists of  $\text{Fe}_2\text{O}_3$  grains and oxide NWs originate from the top of grains. In contrast, GB regions hardly show sign of formation



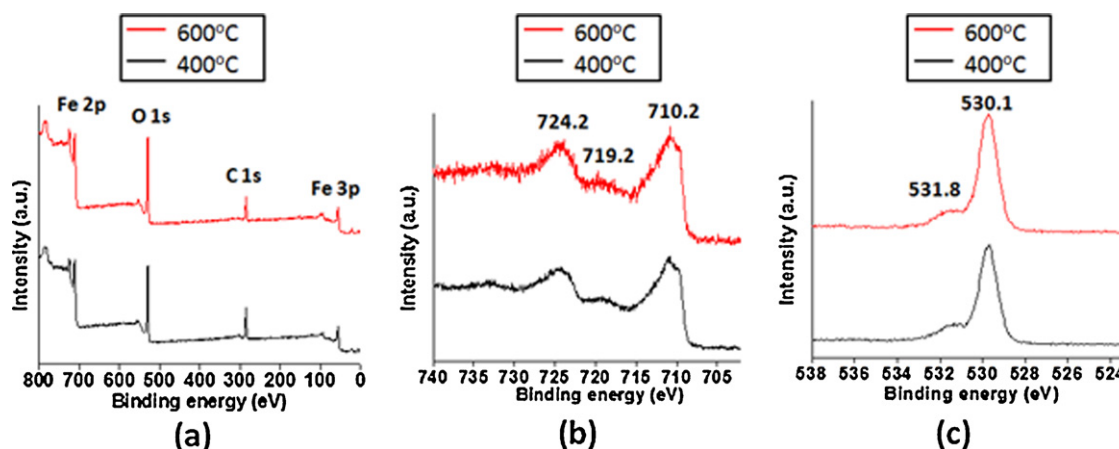


Fig. 4. XPS spectra of  $\text{Fe}_2\text{O}_3$  NWs: (a) wide range spectrum; (b) Fe 2p spectrum; (c) O 1s spectrum.

of NWs. An instructive comparison is the occurrence of tin whisker growth on tin plated Cu lead frames, where whiskers are extruded from the GBs and the cross-sectional shape of whiskers is correlated with the GB geometry at the surface [33]. As revealed from these images, cross-sectional shapes of  $\text{Fe}_2\text{O}_3$  NWs show no correlation with the GB geometry, confirming that the NW formation is not driven by a GB extrusion process.

AFM is employed to examine the growth morphology of the oxide nanowires. Fig. 6(a) is an AFM image showing the initial growth morphology of  $\text{Fe}_2\text{O}_3$  nanowires. It can be noted that the nanowires show a tapered shape at the tip, suggesting the tapered shape growth starts at the very beginning of the nanowire growth. This tapered shape is maintained during the entire growth process, as inferred from the growth morphology of long nanowires that also show a tapered tip (i.e., the inset in Fig. 2). The nanowire sample can be also scratched off the oxidized surface and placed on a flat substrate. Fig. 6(b) shows an AFM image taken from a single  $\alpha\text{-Fe}_2\text{O}_3$  NW lying on a silicon wafer. It can be seen that the diameter of the NW is about 50 nm and is relatively uniform along the length direction.

The microstructure and crystallographic orientations at the interfaces between the different oxide layers are also examined using TEM imaging and selected-area electron diffraction (SAED). Fig. 7 shows a typical bright-field (BF) TEM image from the root region of oxide NWs formed from the oxidation at 600 °C. As can be seen,  $\text{Fe}_2\text{O}_3$  nanowires form directly on the top of  $\text{Fe}_2\text{O}_3$  grains, consistent with the SEM observations. The SAED patterns from an individual NW and its underlying grain on which the NW is

originated reveal that both the nanowire and the underlying grain have the hematite hexagonal structure as depicted in the inset showing diffraction patterns, where the pattern in the left-upper inset is from the nanowire and the pattern in the left-lower inset is from the underlying grain. The  $\text{Fe}_2\text{O}_3$  layer has a polycrystalline structure with an average grain size of  $\sim 100$  nm (this can be also noted from the cross-sectional TEM images in Fig. 11). The SAED pattern obtained from the grain right beneath the  $\text{Fe}_2\text{O}_3$  nanowire shows a single crystal spot pattern. The TEM image contrast reveals the presence of a twin boundary in the nanowire along its axial direction. This is consistent with the SAED pattern in the left-upper inset, which is composed of two sets of diffraction spots owing to the bicrystal structure of the NW. It can be seen from the SAED pattern (lower-left inset) that the  $\text{Fe}_2\text{O}_3$  grain has a single crystal structure. Their different structure features (i.e., twin structure occurs only in the NW) as revealed by the SAED patterns demonstrate clearly that the formation of twin boundary in the NW is not simply a replication of the structure of the underlying  $\text{Fe}_2\text{O}_3$  grain although the twin boundary is observed to start from the NW root and continue into the NW along the axial direction.

The nature of the bicrystal structure of NWs is presented in more detail in Fig. 8. Two sets of the diffraction spots can be noted in the SAED pattern (Fig. 8b), one is along  $[\bar{1}101]$  zone axis and the other has the  $[0001]$  zone axis. The diffraction pattern also reveals that the NW grows along the  $[11\bar{2}0]$  direction. Fig. 8c displays a high-resolution TEM image from the NW, which shows clearly the presence of the twin boundary along the NW axial direction. Fourier transform patterns (Figs. 8d and e) from the two sides of the HRTEM

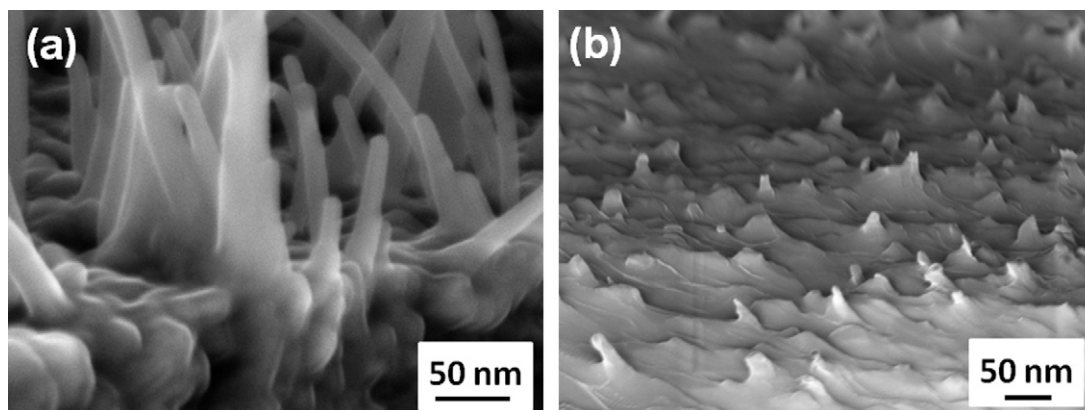
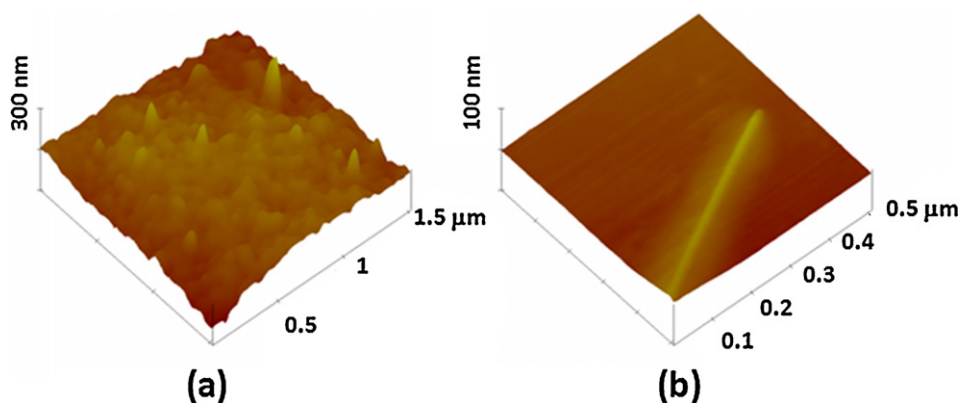


Fig. 5. (a) Cross-sectional SEM micrograph showing the NW root region, (b) SEM image of a Fe substrate oxidized at 400 °C for  $\sim 30$  min, showing the initial growth morphology of  $\text{Fe}_2\text{O}_3$  NWs.



**Fig. 6.** (a) 3D AFM image of the oxidized surface showing the initial growth morphology of  $\text{Fe}_2\text{O}_3$  NWs formed by oxidation at 200 Torr and  $600^\circ\text{C}$  for 30 min; (b) a single  $\alpha\text{-Fe}_2\text{O}_3$  NW lying on a silicon wafer.

image reveal that the left side of the NW is oriented along the  $\text{Fe}_2\text{O}_3$   $[\bar{1}101]$  zone axis while the zone axis for the right side of the NW is along the direction  $\text{Fe}_2\text{O}_3$   $[0001]$ .

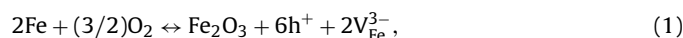
Fig. 9a is a BF TEM image of several grains in the  $\text{Fe}_3\text{O}_4$  layer. As can be noted, grain boundaries are relatively aligned and pores or cracks are formed at some grain boundary areas. No specific crystallographic orientation relationships can be identified among grains in the  $\text{Fe}_3\text{O}_4$  layer although they form a columnar structure. SAED patterns obtained from the corresponding grains are given in Fig. 9b. Indexing of the diffraction patterns indicate that these grains do not form a textured structure, i.e., no common crystallographic orientations among the grains.

Fig. 10a is a BF TEM image obtained from the interface between FeO and the Fe substrate. Large holes are formed at the FeO/Fe interface, caused largely by the stresses generated from the significant volume change accompanying with the oxide formation. This is also consistent with the SEM observations, which reveal that the oxide scales are often detached from the Fe substrate. It can be seen that the FeO layer and Fe substrate have a rough interface morphology with FeO grains embedded partially into the Fe substrate,

suggesting that FeO grains grow into the Fe substrate during the oxidation. Fig. 10b and c are SAED patterns from the Fe substrate and a FeO grain in the oxide layer, their crystallographic orientation relations can be identified as  $[01\bar{1}]_{\text{FeO}}/[01\bar{1}]_{\text{Fe}}$ ,  $[01\bar{1}]_{\text{FeO}}/[0\bar{1}1]_{\text{Fe}}$ , and  $(100)_{\text{FeO}}/(200)_{\text{Fe}}$ .

#### 4. Discussion

Oxide NW growth during metal oxidation has been explained by the stress-driven mechanism [17,34–36]. However, it remains unclear how the compressive stress is generated in the oxide layers in view of the unconstrained oxide growth on the free surface by outward diffusion of Fe cations, where the volume difference between metal and oxides is simply reflected in the scale thickness. Iron forms three thermodynamically stable oxides, FeO,  $\text{Fe}_3\text{O}_4$  and  $\text{Fe}_2\text{O}_3$ , on the reaction with oxygen. Oxide layering can be understood from thermodynamic equilibrium analysis. According to the iron-oxygen phase diagram, the phase wustite (FeO) does not form below  $570^\circ\text{C}$  [37]. Therefore, Fe oxidized below this temperature is expected to form a two-layer structure of  $\text{Fe}_3\text{O}_4$  and  $\text{Fe}_2\text{O}_3$  with the  $\text{Fe}_3\text{O}_4$  next to the Fe substrate. Above  $570^\circ\text{C}$ , the oxide layer sequence in the scale is FeO,  $\text{Fe}_3\text{O}_4$  and  $\text{Fe}_2\text{O}_3$ , with the FeO layer next to Fe. These behaviors of oxide layering are consistent with our oxidation experiments as revealed in Fig. 3. To incorporate gas oxygen into the oxide lattice during the growth of layered oxides, the oxygen first chemisorbs on the  $\text{Fe}_2\text{O}_3$  surface by attracting an electron from a Fe lattice site thus forming an electron hole. The chemisorbed oxygen is fully ionized forming another hole and a  $\text{Fe}^{3+}$  ion enters the surface to partner the  $\text{O}^{2-}$ , thus forming another hole and a vacancy in the cation sub-lattice. Therefore, Fe cation vacancies and electron holes are created at the  $\text{Fe}_2\text{O}_3$  surface and this occurs when  $\text{O}_2$  at the  $\text{Fe}_2\text{O}_3$  surface utilizes  $\text{Fe}^{3+}$  ions from the outer  $\text{Fe}_2\text{O}_3$  lattice to form new  $\text{Fe}_2\text{O}_3$  molecules, in accordance with the reaction [38]



where  $\text{h}^+$  represents an electron hole having an effective charge  $e^+$  and  $\text{V}_{\text{Fe}}^{3-}$  represents a cation vacancy having an effective negative charge of  $3e^-$ . The cation vacancies and electron holes so produced migrate through the  $\text{Fe}_2\text{O}_3$ ,  $\text{Fe}_3\text{O}_4$ , and FeO layers, being annihilated finally at the FeO/Fe interface. Similarly, the phase-boundary reactions at the  $\text{Fe}_2\text{O}_3/\text{Fe}_3\text{O}_4$  and  $\text{Fe}_3\text{O}_4/\text{FeO}$  interfaces during growth of the  $\text{Fe}_3\text{O}_4$  and FeO layers also generates new cation vacancies and electron holes, which migrate through the  $\text{Fe}_3\text{O}_4$  and FeO layer and are annihilated at the parent metal of Fe. These defect species originate in the solid-state reactions in which the oxygen-rich layer (i.e.,  $\text{Fe}_2\text{O}_3$  layer) undergoes decomposition to form more oxide

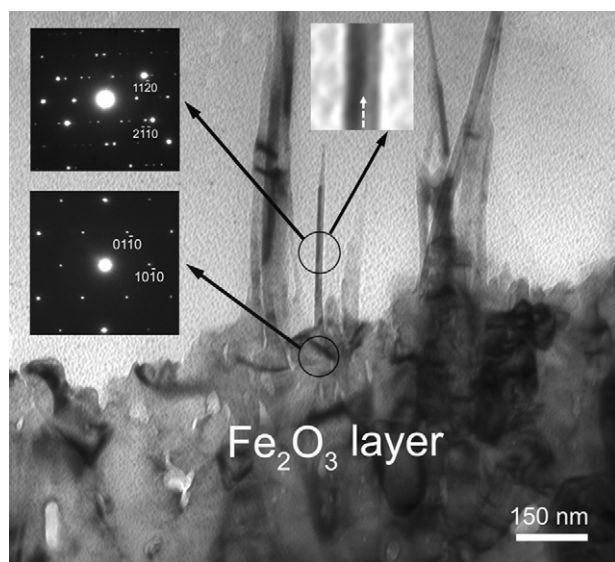


**Fig. 7.** Cross-sectional BF TEM image showing the NW root region and the underlying  $\text{Fe}_2\text{O}_3$  layer. Inset shows selected area electron diffraction (SAED) patterns from the NW and the underlying  $\text{Fe}_2\text{O}_3$  grain. Both the NW and grain have the hexagonal hematite structure. The NW contrast from the closer-view image (inset) suggests the presence of a twin boundary along the axial direction of the NW, consistent with the SAED pattern (upper-left inset) from the NW.

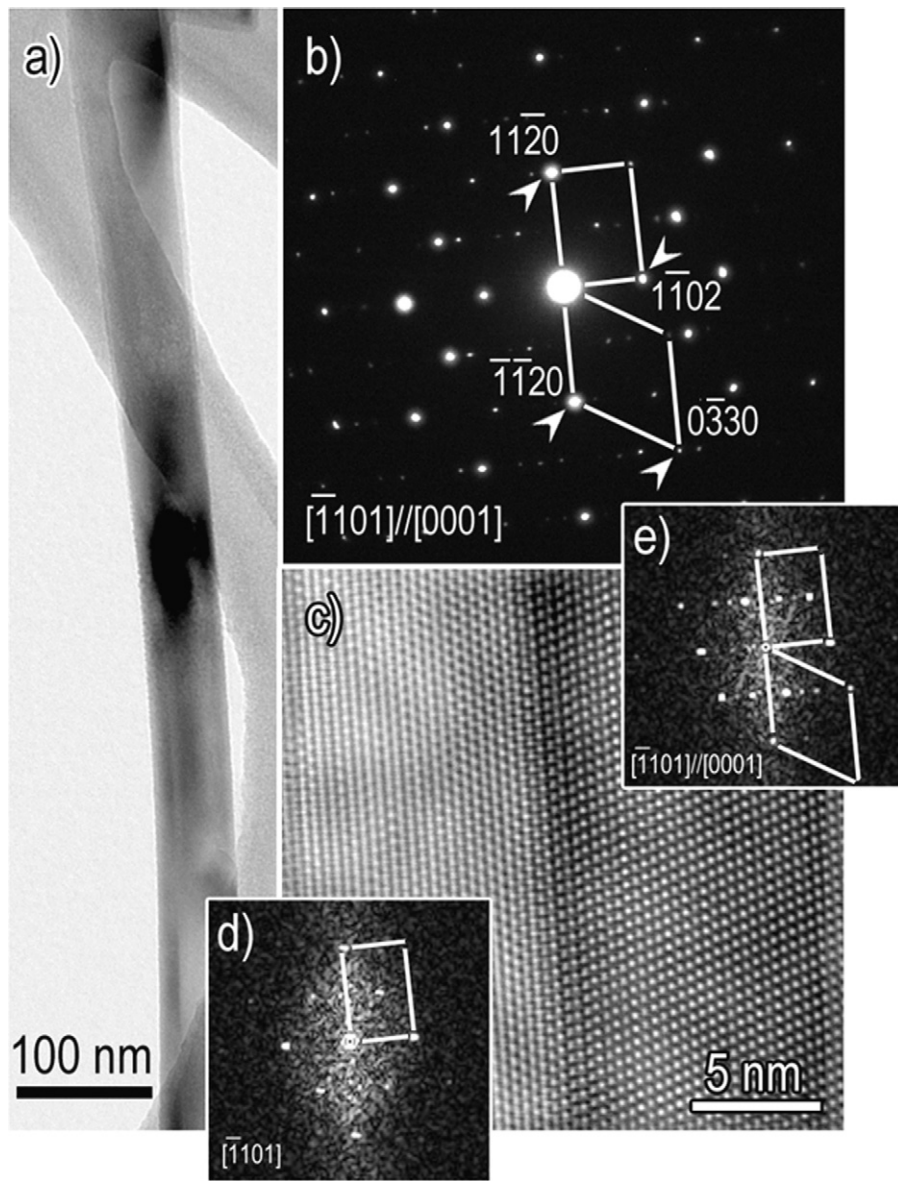
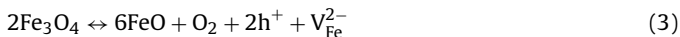
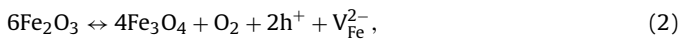


**Fig. 8.** (a) BF TEM image of a  $\text{Fe}_2\text{O}_3$  nanowire. (b) SAED obtained from the NW, indexing of the pattern reveals two sets of different points with the zone axes of  $[\bar{1}101]$  and  $[0001]$ , respectively. (c) HRTEM image of the NW confirms the presence of the twin boundary. (d and e) Fourier transform patterns from left and right side of the HRTEM image.

of the  $\text{Fe}_3\text{O}_4$  layer at the  $\text{Fe}_2\text{O}_3/\text{Fe}_3\text{O}_4$  interface and meanwhile the  $\text{Fe}_3\text{O}_4$  layer undergoes decomposition to form more FeO at the  $\text{Fe}_3\text{O}_4/\text{FeO}$  interface in accordance with the following reactions,



where  $\text{V}_{\text{Fe}}^{2-}$  represents cation vacancies in  $\text{Fe}_3\text{O}_4$  and FeO layers. Cation vacancies, together with electron holes  $\text{h}^+$ , are produced by the solid-state transformations for increasing the thicknesses of the  $\text{Fe}_3\text{O}_4$  and FeO layers, i.e., growth of the FeO layer requires decomposition of the oxygen-rich  $\text{Fe}_3\text{O}_4$  layer to obtain the necessary oxygen while growth of the  $\text{Fe}_3\text{O}_4$  layer requires decomposition of the oxygen-rich  $\text{Fe}_2\text{O}_3$  layer. All cation vacancies generated in the reactions given by Eqs. (1)–(3) eventually flow to the parent Fe for annihilation, accompanied by an equivalent outward flow of cations (i.e., the overall reaction is limited by the diffusion of Fe ions through a vacancy mechanism [37]). The wustite phase, FeO, can exist with high cation vacancy concentrations at high

temperatures, and the mobilities of cations and electrons are extremely high [37]. This explains why the FeO layer is much thicker than the other two oxide layers.  $\text{Fe}_3\text{O}_4$  is an inverse spinel and has divalent ions  $\text{Fe}^{2+}$  occupying octahedral sites and half of the trivalent ions  $\text{Fe}^{3+}$  occupying tetrahedral sites. Defects occur on both sites and, consequently, Fe ions can diffuse efficiently over both tetrahedral and octahedral sites, resulting in the much thicker  $\text{Fe}_3\text{O}_4$  layer than the  $\text{Fe}_2\text{O}_3$  layer (Fig. 3b).

The Pilling and Bedworth's ratios (the ratio of the volume of the metal oxide, which is produced by the reaction of metal and oxygen, to the volume of consumed metal) for FeO,  $\text{Fe}_3\text{O}_4$ , and  $\text{Fe}_2\text{O}_3$ , are 1.68, 2.10, and 2.14, respectively [39]. Due to their different specific volumes, the ensuring difficulties in local volume accommodation accompanying the solid-state transformations at the  $\text{Fe}_2\text{O}_3/\text{Fe}_3\text{O}_4$ ,  $\text{Fe}_3\text{O}_4/\text{FeO}$ , and FeO/Fe interfaces result in generation of stresses at the interfacial regions. Since both the  $\text{Fe}_3\text{O}_4$  and FeO layers have large thickness ( $>2\text{ }\mu\text{m}$ ), and the stresses generated at the Fe/FeO and  $\text{Fe}_3\text{O}_4/\text{FeO}$  interfaces can be released by a number mechanisms including cracking and spalling of the oxide scales and plastic



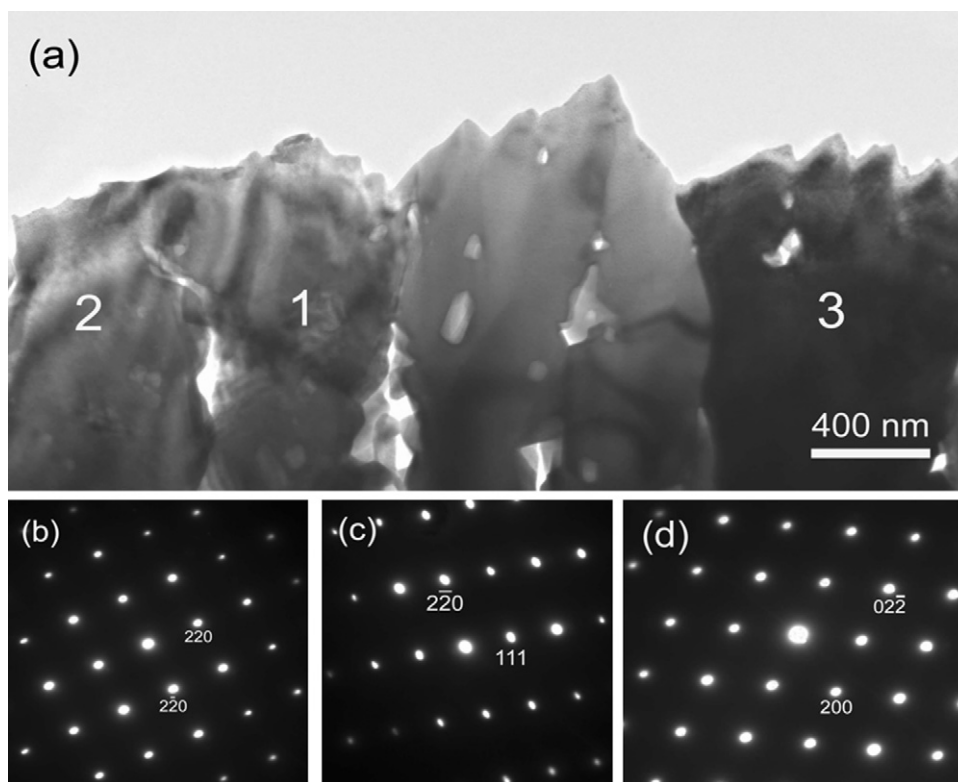


**Fig. 9.** (a) BF TEM image of oxide grains in the  $\text{Fe}_3\text{O}_4$  layer, (b–d) SAED patterns from the grain 1, 2 and 3 in (a), respectively.

deformation of the oxide and the Fe substrate. This can be evidenced from the formation of cracks in the  $\text{FeO}$  and  $\text{Fe}_3\text{O}_4$  layers as well as the frequently observed detachment of the oxide scale from the Fe substrate, as shown in Figs. 3, 9 and 10.

$\text{Fe}_2\text{O}_3$  NW growth is mainly associated with the stress generation and relaxation at the  $\text{Fe}_2\text{O}_3/\text{Fe}_3\text{O}_4$  interface.  $\text{Fe}_3\text{O}_4$  grows

at the expense of the thin  $\text{Fe}_2\text{O}_3$  layer via the continuous oxide-forming reaction at the  $\text{Fe}_2\text{O}_3/\text{Fe}_3\text{O}_4$  interface. Since the specific volume of  $\text{Fe}_2\text{O}_3$  is slightly larger than that of  $\text{Fe}_3\text{O}_4$ , compressive stresses are generated and accumulated in the  $\text{Fe}_2\text{O}_3$  interface region due to the volume shrinkage associated with the conversion of  $\text{Fe}_2\text{O}_3$  into  $\text{Fe}_3\text{O}_4$ . Fig. 11 shows cross-sectional TEM images

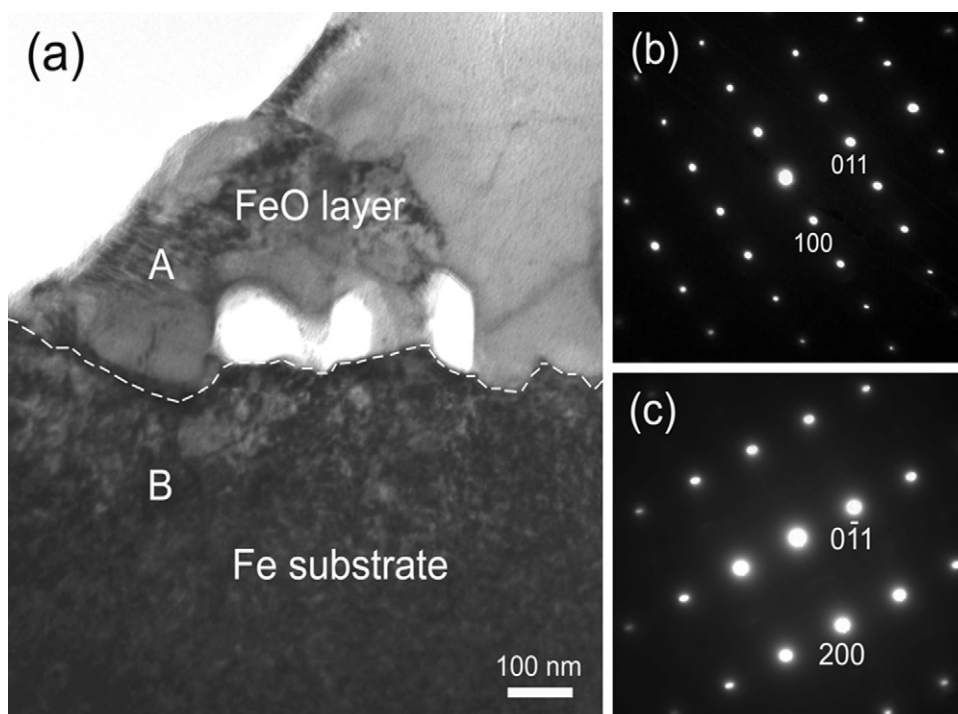


**Fig. 10.** (a) BF TEM image of the  $\text{FeO}/\text{Fe}$  interface region, (b) SAED pattern from the grain A in the  $\text{FeO}$  layer, and (c) SAED pattern from the grain B in the Fe substrate.

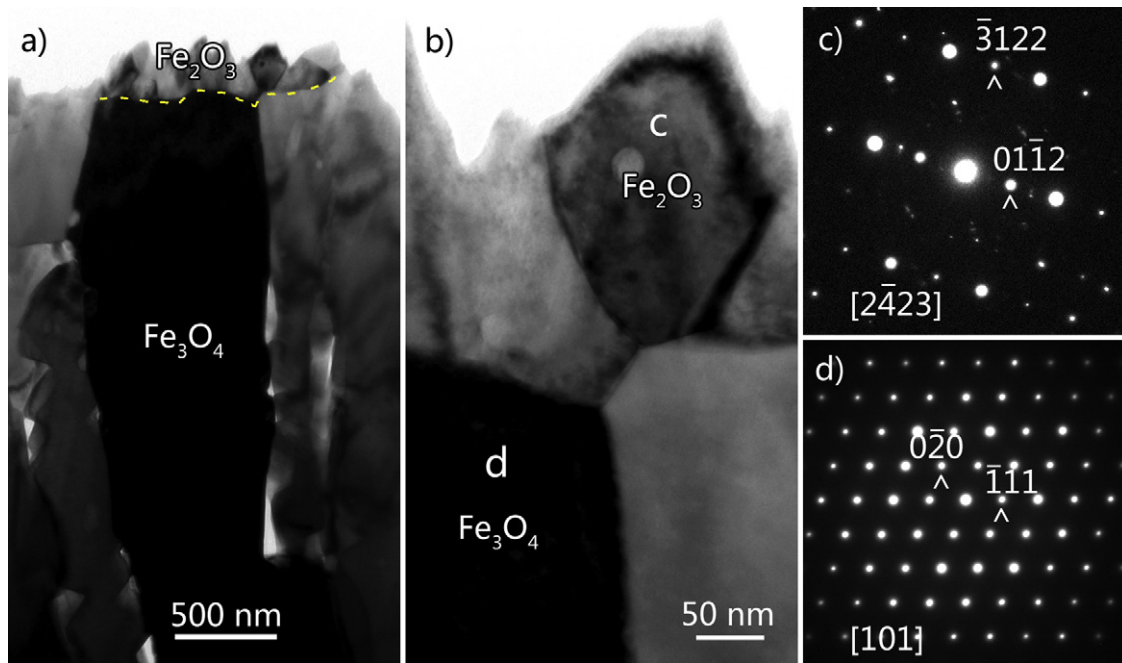


**Fig. 11.** (a) BF TEM image of the  $\text{Fe}_2\text{O}_3/\text{Fe}_3\text{O}_4$  interface region, cracks are formed along the grain boundary regions in the  $\text{Fe}_3\text{O}_4$  layer; (b) closer-view near the  $\text{Fe}_2\text{O}_3/\text{Fe}_3\text{O}_4$  interface region revealing the intact grain structure in the  $\text{Fe}_2\text{O}_3$  layer; (c and d) SAED patterns confirming the crystal structures of grains as indicated by (c) and (d), respectively, in the two oxide layers.

from the  $\text{Fe}_2\text{O}_3/\text{Fe}_3\text{O}_4$  interface, which reveals clearly that  $\text{Fe}_2\text{O}_3$  grains are intact and do not exhibit cracking while the  $\text{Fe}_3\text{O}_4$  layer contains pores and cracking along the grain boundaries away from the interface area. This suggests that the stresses generated at the  $\text{Fe}_2\text{O}_3/\text{Fe}_3\text{O}_4$  interface are released by a mechanism different from that of  $\text{Fe}_3\text{O}_4/\text{FeO}$  and  $\text{FeO}/\text{Fe}$  interfacial reactions. Our observations have indicated that the thickness of the  $\text{Fe}_2\text{O}_3$  layer on which  $\text{Fe}_2\text{O}_3$  NW formation occurs is about 400 nm or less (see Figs. 3 and 11). This implies a process that sets limitation on the thickness of the  $\text{Fe}_2\text{O}_3$  layer for effective relaxation of the compressive stresses. Since the  $\text{Fe}_2\text{O}_3$  layer is very thin and has much smaller grain sizes (and therefore more grain boundaries in the oxide layer) than the  $\text{Fe}_3\text{O}_4$  layer, the  $\text{Fe}_2\text{O}_3$  layer is believed to provide paths to release the stress via outward grain boundary diffusion, where Fe ions diffuse along grain boundaries from the region in compression (i.e., near the  $\text{Fe}_2\text{O}_3/\text{Fe}_3\text{O}_4$  interface) to the outer surface of the  $\text{Fe}_2\text{O}_3$  layer, which is stress free. The diffusive flux  $J_{\text{GB}}$  driven by the stress gradient follows Eq. (4) [40]. Here  $\sigma$  is the compressive stress,  $D_{\text{GB}}$  is the grain boundary diffusion coefficient,  $\delta$  the grain boundary width,  $k$  Boltzmann's constant,  $T$  the absolute temperature,  $\Omega$  is the atomic volume of an Fe ion in  $\alpha\text{-Fe}_2\text{O}_3$ , and  $s$  is the local spatial coordinate along the diffusion path.

$$J_{\text{GB}} = \frac{D_{\text{GB}}\delta\Omega}{kT} \frac{\partial\sigma_n}{\partial s} \quad (4)$$

Fe cations diffusing along the GBs are deposited on the  $\text{Fe}_2\text{O}_3$  grains via surface diffusion, where existing  $\text{Fe}_2\text{O}_3$  grains serve as the structure template for  $\text{Fe}_2\text{O}_3$  NW nucleation. Such a process leads to the nucleation of NWs on the top of  $\text{Fe}_2\text{O}_3$  grains, as evidenced in Figs. 5 and 7, which shows that  $\text{Fe}_2\text{O}_3$  NWs are formed on grains rather than from grain boundary regions. The NW growth is surface diffusion driven by concentration gradients of Fe ions between the NW root and the NW tip and grain boundary junction areas where Fe ions are delivered onto the surface via grain boundary diffusion. Previous studies have shown that  $\text{Fe}_2\text{O}_3$  grows at the tip [41]. The tapered shape of NW tips as observed in our case (see Figs. 2 and 6) confirm the tip growth mechanism, where arriving Fe ions via surface diffusion are incorporated into atomic steps

present near the NW tip. The bi-crystal structure of the NW originates from the surface facets of  $\text{Fe}_2\text{O}_3$  grains on which  $\text{Fe}_2\text{O}_3$  NWs nucleate and grow. The crystals grown on the different facets of a  $\text{Fe}_2\text{O}_3$  grain are naturally merged together to form a twin or multi-twin structure starting from the grain top and continuing into the NW along the axial direction. The mass transport mechanisms and paths of Fe diffusion to support the NW growth are schematically shown in Fig. 12. The outward diffusion flux of Fe atoms as a continual source of Fe cations for  $\text{Fe}_2\text{O}_3$  NW growth continues as long as the compressive stress in the  $\text{Fe}_2\text{O}_3$  layer is maintained by the solid-state phase transformation (i.e., Eq. (2)) at the  $\text{Fe}_2\text{O}_3/\text{Fe}_3\text{O}_4$  interface.

Since a fraction of Fe atoms delivered onto the outer surface of the  $\text{Fe}_2\text{O}_3$  layer by GB diffusion are directly incorporated into the  $\text{Fe}_2\text{O}_3$  substrate, only the remaining Fe atoms are transferred onto the side wall of the NW via adatom-NW exchange by surface diffusion. Following the similar treatment [42–44], we have obtained the growth kinetics of  $\text{Fe}_2\text{O}_3$  NWs via the surface diffusion by [30]

$$t = \frac{\lambda_w^2 R}{2D_w\Omega(n_s^\infty - n_w^0)} \ln \left[ \cosh \left( \frac{h}{\lambda_w} \right) + \beta^{-1} \sinh \left( \frac{h}{\lambda_w} \right) \right], \quad (5)$$

where  $t$  is the oxidation time,  $D_w$ ,  $\tau_w$ , and  $\lambda_w$  are the diffusivity, diffusion time, and surface diffusion length of Fe ions on the NW, respectively,  $\Omega$  is the atomic volume of a Fe ion,  $n_w^\infty$  are the concentration of Fe ions delivered by grain boundary diffusion onto the substrate and  $n_w^0$  is the concentration of Fe ions at the NW tip in equilibrium with the oxygen gas,  $R$  is the radius of the NW,  $h$  is the NW length, and  $\beta$  is a parameter describing the ratios of surface diffusion of Fe ions on the  $\alpha\text{-Fe}_2\text{O}_3$  substrate and along the sidewall of an  $\alpha\text{-Fe}_2\text{O}_3$  nanowire [30]. Eq. (5) gives the NW length  $h$  as a function of NW diameter  $R$  for a period of growth time  $t$  at the constant oxidation temperature and oxygen pressure. Eq. (5) suggests that thinner nanowires are longer than thicker ones for a fixed oxidation time  $t$ . Fig. 13 shows the experimental NW lengths vs. the radii of individual NWs measured from SEM images of the Fe samples oxidized at 600 °C with two different oxidation durations. A scattered distribution of the experimental data is noted and this may be due



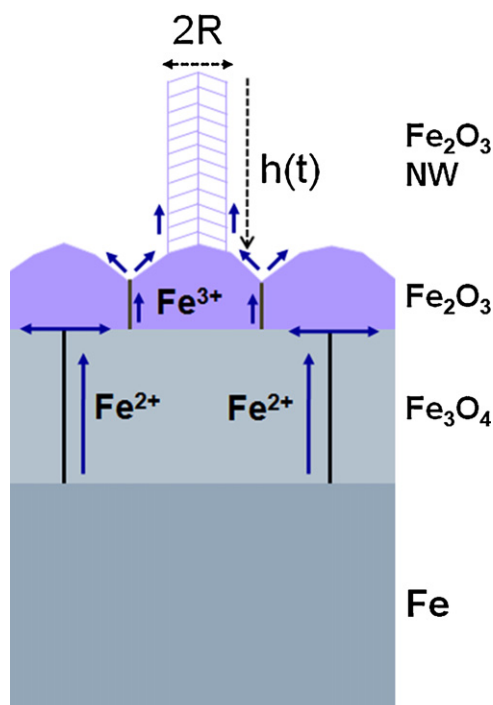


**Fig. 12.** Schematic showing the path of Fe diffusion to support the NW: Fe ions diffuse outward from the  $\text{Fe}_2\text{O}_3/\text{Fe}_3\text{O}_4$  interface to the free surface via grain boundary diffusion driven by the  $\text{Fe}_2\text{O}_3/\text{Fe}_3\text{O}_4$  interfacial reaction, followed by surface diffusion from grain boundary junction areas to the NW root and then to the NW tip driven by the concentration gradient.

to the fact that not all NWs are nucleated at the same time. The solid curves correspond to the theoretical fitting using Eq. (4) with the fitting parameters of  $2D_w\Omega(n_z^\infty - n_w^0)/\lambda_w^2 = 0.1 \text{ nm/min}$ ,  $\beta^{-1} = 0.1$ , and  $\lambda_w = 2701 \text{ nm}$ . The general trend between the experimental data and the kinetic model agrees well, i.e., thinner NWs are longer than thicker ones.  $D_w$  cannot be determined from the fitting parameter since  $n_z^\infty$  and  $n_w^0$  are unknown, however,  $\lambda_w$  has a reasonable value for surface diffusion for the elevated temperature (i.e.,  $600^\circ\text{C}$ ).

The growth of oxide NWs or platelets has been observed from the oxidation of many other metal and alloy systems including Cu [17–21], Ni [45], Mo [7], Zn [22], Fe–Ni [5]. A noticeable feature for the oxide NW formation during the oxidation is the requirement

for a thin oxide layer present on the outer surface. Thin layers are known to be more intensively stressed and more readily produce whiskers. The stress gradient occurs due to the volume changes accompanying the interfacial reaction and acts as a thermodynamic driving force for oxide NW growth. Besides the oxidation-induced stress gradient, it is also noted that thermal expansion mismatch can be employed to generate similar stress gradient between the overlayer film and the substrate, resulting in a flux of material to the low stress surface for nanowire growth upon heating [46–48]. These observations indicate that a similar wire growth mechanism, i.e., stress-driven nanowire formation, may be possible in layered systems, where biaxial compressive stresses can be introduced via solid-state interfacial reaction (e.g., oxidation), heating, or other means.

## 5. Conclusions

Iron-oxide scaling leading to hematite ( $\alpha\text{-Fe}_2\text{O}_3$ ) nanowire growth has been investigated in order to better understand this specific oxide growth. The main observations and conclusions can be summarized as follows: (1) Fe can be oxidized to  $\text{Fe}/\text{FeO}/\text{Fe}_3\text{O}_4/\text{Fe}_2\text{O}_3$  or  $\text{Fe}/\text{Fe}_3\text{O}_4/\text{Fe}_2\text{O}_3$  layered structures, depending on the oxidation temperature.  $\text{Fe}_2\text{O}_3$  NW growth occurs for both the three-layered and four-layered structures. (2) The driving force leading to the spontaneous  $\text{Fe}_2\text{O}_3$  NW formation is attributed to the relaxation of the compressive stresses generated from the solid-state transformation at the  $\text{Fe}_3\text{O}_4/\text{Fe}_2\text{O}_3$  interface. Fe atom transport occurs via grain boundary diffusion from the compressed regions at the  $\text{Fe}_2\text{O}_3/\text{Fe}_3\text{O}_4$  interface region to the outer surface of the  $\text{Fe}_2\text{O}_3$  layer, which is stress free. (3) The requirement for effective releasing the interfacial stresses sets a limit on the thickness of the  $\text{Fe}_2\text{O}_3$  outer layer, which is observed to be less than  $400 \text{ nm}$  for initiating  $\text{Fe}_2\text{O}_3$  NW formation. (4)  $\text{Fe}_2\text{O}_3$  NWs originate from the top of  $\text{Fe}_2\text{O}_3$  grains rather than the grain boundaries regions, and the formation of twin boundaries is attributed to the initial nucleation and growth stages of the NW on the different surface facets of the underlying  $\text{Fe}_2\text{O}_3$  grain. (5)  $\text{Fe}_2\text{O}_3$  NWs grow at their tip, where Fe cations are supplied by the substrate–NW adatom exchange via surface diffusion. (6) The similarity of the oxidation-induced layered structure with other layered systems suggests the broad applicability of the stress-driven NW formation mechanism.

## Acknowledgements

This work was supported by National Science Foundation Grant No. CMMI-0825737. Y.Q. Wang would like to thank the financial support from the National Natural Science Foundation of China (Grant No. 10974105) and the Natural Science Foundation for Outstanding Young Scientists in Shandong Province, China (Grant No. JQ201002).

## References

- [1] R.M. Cornell, U. Schwertmann, *The Iron Oxides: Structure, Properties, Reactions, Occurrences and Uses*, Wiley-VCH, New York, 2003.
- [2] S.Q. Liu, K.L. Huang, Straightforward fabrication of highly ordered  $\text{TiO}_2$  nanowire arrays in AAM on aluminum substrate, *Sol. Energy Mater. Sol. Cells* 85 (2005) 125–131.
- [3] J. Chen, L. Xu, W. Li, X. Gou,  $\alpha\text{-Fe}_2\text{O}_3$  nanotubes in gas sensor and lithium-ion battery applications, *Adv. Mater.* 17 (2005) 582–586.
- [4] T. Tepper, F. Ilievski, C.A. Ross, T.R. Zaman, R.J. Ram, S.Y. Yung, B. Stadler, *J. Appl. Phys.* 93 (2003) 6948.
- [5] Y.L. Chueh, M.W. Lai, J.Q. Liang, L.J. Chou, Z.L. Wang, Systematic study of the growth of aligned arrays of  $\alpha\text{-Fe}_2\text{O}_3$  and  $\text{Fe}_3\text{O}_4$  nanowires by a vapor-solid process, *Adv. Funct. Mater.* 16 (2006) 2243–2251.
- [6] Y.Y. Fu, J. Chen, J. Zhang, Synthesis of  $\text{Fe}_2\text{O}_3$  nanowires by oxidation of iron, *Chem. Phys. Lett.* 350 (2001) 491–494.

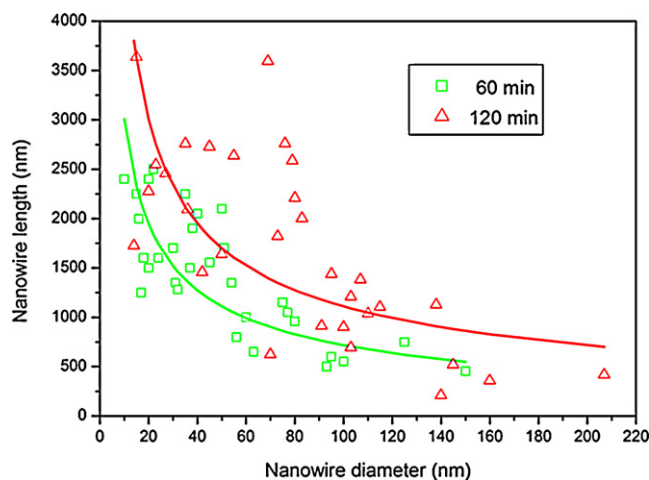


**Fig. 13.** NW lengths vs. the radii measured from individual NWs formed from the oxidation at  $400^\circ\text{C}$  for 60 min and 120 min, where solid lines are model fitting to experimental values of the NW lengths and diameters.

- [7] S. Rachauskas, A.G. Nasibulin, H. Jiang, Y. Tian, V.I. Kleshch, J. Sainio, E.D. Obratsova, S.N. Bokova, A.N. Obratsov, E.I. Kauppinen, A novel method for metal oxide nanowire synthesis, *Nanotechnology* 20 (2009) 165603.
- [8] A.G. Nasibulin, S. Rackauskas, H. Jiang, Y. Tian, P.R. Mudimela, S.D. Shandakov, L.I. Nasibulina, J. Sainio, E.I. Kauppinen, Simple and rapid synthesis of  $\alpha$ -Fe<sub>2</sub>O<sub>3</sub> nanowires under ambient conditions, *Nano Research* 2 (2009) 373–379.
- [9] R.M. Wang, Y.F. Chen, Y.Y. Fu, H. Zhang, C. Kisielowski, Bicrystalline hematite nanowires, *J. Phys. Chem. B* 109 (2005) 12245–12249.
- [10] Q. Han, Z.H. Liu, Y.Y. Xu, Z.Y. Chen, T.M. Wang, H. Zhang, Growth and properties of single-crystalline  $\gamma$ -Fe<sub>2</sub>O<sub>3</sub> nanowires, *J. Phys. Chem. C* 111 (2007) 5034–5038.
- [11] Z. Dong, P. Kashkarov, H. Zhang, Monte Carlo study for the growth of  $\alpha$ -Fe<sub>2</sub>O<sub>3</sub> nanowires synthesized by thermal oxidation of iron, *Nanoscale* 2 (2010) 524–528.
- [12] H. Srivastava, P. Tiwari, A.K. Srivastava, R.V. Nandedkar, Growth and characterization of  $\alpha$ -Fe<sub>2</sub>O<sub>3</sub> nanowires, *J. Appl. Phys.* 102 (2007) 054303.
- [13] P. Hiralal, H.E. Unalan, K.G.U. Wijayantha, A. Kursumovic, D. Jefferson, J.L. MacManus-Driscoll, G.A.J. Amaratunga, Growth and process conditions of aligned and patternable films of iron (III) oxide nanowires by thermal oxidation of iron, *Nanotechnology* 19 (2008) 455608.
- [14] U. Cvelbar, Z.Q. Chen, M.K. Sunkara, M. Mozetic, Spontaneous growth of superstructure  $\alpha$ -Fe<sub>2</sub>O<sub>3</sub> nanowire and nanobelt arrays in reactive oxygen plasma, *Small* 4 (2008) 1610–1614.
- [15] X.G. Wen, S.H. Wang, Y. Ding, Z.L. Wang, S.H. Yang, Controlled growth of large-area, uniform, vertically aligned arrays of  $\alpha$ -Fe<sub>2</sub>O<sub>3</sub> nanobelts and nanowires, *J. Phys. Chem. B* 109 (2005) 215–220.
- [16] Z.Q. Chen, U. Cvelbar, M. Mozetic, J.Q. He, M.K. Sunkara, Long-range ordering of oxygen-vacancy planes in  $\alpha$ -Fe<sub>2</sub>O<sub>3</sub> nanowires and nanobelts, *Chem. Mater.* 20 (2008) 3224–3228.
- [17] A.M. Goncalves, L.C. Campos, A.S. Ferlauto, R.G. Lacerda, On the growth and electrical characterization of CuO nanowires by thermal oxidation, *J. Appl. Phys.* 106 (2009) 034303.
- [18] X.C. Jiang, T. Herricks, Y.N. Xia, CuO nanowires can be synthesized by heating copper substrates in air, *Nano Letters* 2 (2002) 1333–1338.
- [19] N. Chopra, B. Hu, B. Hinds, Selective growth and kinetic study of copper oxide nanowires from patterned thin-film multilayer structures, *J. Mater. Res.* 22 (2007) 269–2699.
- [20] B.J. Hansen, H.I. Chan, J. Lu, G.H. Lu, J.H. Chen, Short-circuit diffusion growth of long bi-crystal CuO nanowires, *Chem. Phys. Lett.* 504 (2011) 4–45.
- [21] E. Comini, C. Baratto, G. Faglia, M. Ferroni, A. Vomiero, G. Sberveglieri, Quasi-one dimensional metal oxide semiconductors: preparation, characterization and application as chemical sensors, *Progress in Materials Science* 54 (2009) 1–67.
- [22] Y.H. Sun, J.Y. Gao, R. Zhu, J. Xu, L. Chen, J.M. Zhang, Q. Zhao, D.P. Yu, In situ observation of ZnO nanowire growth on zinc film in an environmental scanning electron microscope, *J. Chem. Phys.* 132 (2010) 124705.
- [23] I. Avramov, Kinetics of growth of nanowhiskers (nanowires and nanotubes), *Nanoscale Res. Lett.* 2 (2007) 235–239.
- [24] X. Jiang, T. Herricks, Y. Xia, CuO nanowires can be synthesized by heating copper substrates in air, *Nano Letters* 2 (2002) 1333–1338.
- [25] D. Voss, E. Butler, T. Mitchell, The growth of hermatite blades during the high temperature oxidation of Iron, *Metall. Mater. Trans. A* 13 (1982) 929–935.
- [26] B.J. Hansen, H.-I. Chan, J. Lu, G. Lu, J. Chen, Short-circuit diffusion growth of long bi-crystal CuO nanowires, *Chem. Phys. Lett.* 504 (2011) 41–45.
- [27] J.T. Chen, F. Zhang, J. Wang, G.A. Zhang, B.B. Miao, X.Y. Fan, D. Yan, P.X. Yan, CuO nanowires synthesized by thermal oxidation route, *J. Alloys Compd.* 454 (2008) 268–273.
- [28] D.A. Voss, E.P. Bulter, T.E. Michell, The growth of hermatite blades during the high temperature oxidation of iron, *Metall. Trans. A* 13A (1982) 929.
- [29] Q. Han, Y.Y. Xu, Y.Y. Fu, H. Zhang, R.M. Wang, T.M. Wang, Z.Y. Chen, Defects and growing mechanisms of  $\alpha$ -Fe<sub>2</sub>O<sub>3</sub> nanowires, *Chem. Phys. Lett.* 431 (2006) 100–103.
- [30] L. Yuan, Y.Q. Wang, R. Mema, G.W. Zhou, Driving force and growth mechanism for spontaneous oxide nanowire formation during the thermal oxidation of metals, *Acta Mater.* 59 (2011) 2491–2500.
- [31] R. Mema, L. Yuan, Q. Du, Y. Wang, G.W. Zhou, Effect of surface stresses on CuO nanowire growth in the thermal oxidation of copper, *Chem. Phys. Lett.* 512 (2011) 87–91.
- [32] M. Aronniemi, J. Sainio, J. Lahtinen, Chemical state quantification of iron and chromium oxides using XPS: the effect of the background subtraction method, *Surf. Sci.* 578 (2005) 108–123.
- [33] M.W. Barsoun, E.N. Hoffman, R.D. Doherty, S. Gupta, A. Zavaliangos, Driving force and mechanism for spontaneous metal whisker formation, *Phys. Rev. Lett.* 93 (2004) 206104.
- [34] M. Kaur, K.P. Muthe, S.K. Deshpande, S. Choudhury, J.B. Singh, N. Verma, S.K. Gupta, J.V. Yakhmi, Growth and branching of CuO nanowires by thermal oxidation of copper, *J. Cryst. Growth* 289 (2006) 670–675.
- [35] F. Morin, Copious whisker growth on copper scale, *J. Mater. Sci. Lett.* 2 (1983) 383–384.
- [36] A. Kumar, A.K. Srivastava, P. Tiwari, R.V. Nandedkar, The effect of growth parameters on the aspect ratio and number density of CuO nanorods, *J. Phys.: Condens. Matter* 16 (2004) 8531–8543.
- [37] N. Birks, G.H. Meier, F.S. Pettit, Introduction to the High Temperature Oxidation of Metals, 2nd edn., Cambridge, Cambridge University Press, 2006.
- [38] A.T. Fromhold, R.G. Fromhold, An overview of metal oxidation theory, in: C.H. Bamford, C.F.H. Tipper, R.G. Compton (Eds.), *Reactions of Solids with Gases*, vol. 21, Elsevier, New York, 1984.
- [39] M. Schutze, *Protective Oxide Scales and their Breakdown*, John Wiley and Sons, West Sussex, England, 1997.
- [40] A.C.F. Cooks, A finite element description of grain boundary diffusion processes in ceramic materials, in: I.M. Allison, C. Ruiz (Eds.), *Applied Solid Mechanics*, 3 edn., North Holland, Amsterdam, 1989, 30 p.
- [41] R. Takagi, Growth of oxide whiskers on metals at high temperature, *J. Phys. Soc. Jpn.* 12 (1957) 1212.
- [42] V. Ruth, J.P. Hirth, Kinetics of diffusion-controlled whisker growth, *J. Chem. Phys.* 41 (1964) 3139–3149.
- [43] J. Johansson, C.P.T. Svensson, T. Martensson, L. Samuelson, W. Seifert, Mass transport model for semiconductor nanowire growth, *J. Phys. Chem. B* 109 (2005) 13567–13571.
- [44] S.A. Dayeh, E.T. Yu, D.L. Wang, Surface diffusion and substrate-nanowire adatom exchange in InAs nanowire growth, *Nano Letters* 9 (2009) 1967–1972.
- [45] L.C. Dufour, F. Morin, The growth of oxide platelets on nickel in pure oxygen. II. Surface analysis and growth mechanism, *Oxid. Met.* 39 (1992) 137–154.
- [46] J.H. Ham, W. Shim, D.H. Kim, S.H. Lee, J.W. Roh, S.W. Sohn, K.H. Oh, P.W. Voorhees, W.Y. Lee, Direct growth of compound semiconductor nanowires by on-film formation of nanowires: bismuth telluride, *Nano Letters* 9 (2009) 2867–2872.
- [47] W. Shim, J.H. Ham, K.I. Lee, W.Y. Jeung, M. Johnson, W.Y. Lee, On-film formation of Bi nanowires with extraordinary electron mobility, *Nano Letters* 9 (2009) 18–22.
- [48] S.M. Prokes, S. Arnold, Stress-driven formation of Si nanowires, *Appl. Phys. Lett.* 86 (2005) 193105.